land

MDPI

Article

Simulation and Spatio-Temporal Analysis of Soil Erosion in the Source Region of the Yellow River Using Machine Learning Method

Jinxi Su [1,2], Rong Tang [1,2] and Huilong Lin [1,2,*]

[1] State Key Laboratory of Herbage Improvement and Grassland Agro-Ecosystems, College of Pastoral Agriculture Science and Technology, Lanzhou University, Lanzhou 730020, China; sujx2023@lzu.edu.cn (J.S.); tangr19@lzu.edu.cn (R.T.)
[2] Key Laboratory of Grassland Livestock Industry Innovation, College of Pastoral Agriculture Science and Technology, Lanzhou University, Lanzhou 730020, China
* Correspondence: linhuilong@lzu.edu.cn

Abstract: The source region of the Yellow River (SRYR), known as the "Chinese Water Tower", is currently grappling with severe soil erosion, which jeopardizes the sustainability of its alpine grasslands. Large-scale soil erosion monitoring poses a significant challenge, complicating global efforts to study soil erosion and land cover changes. Moreover, conventional methods for assessing soil erosion do not adequately address the variety of erosion types present in the SRYR. Given these challenges, the objectives of this study were to develop a suitable assessment and prediction model for soil erosion tailored to the SRYR's needs. By leveraging soil erosion data measured by ^{137}Cs from 521 locations and employing the random forest (RF) algorithm, a new soil erosion model was formulated. Key findings include that: (1) The RF soil erosion model significantly outperformed the revised universal soil loss equation (RUSLE) model and revised wind erosion equation (RWEQ) model, achieving an R^2 of 0.52 and an RMSE of 5.88. (2) The RF model indicated that from 2001 to 2020, the SRYR experienced an average annual soil erosion modulus (SEM) of 19.32 $t \cdot ha^{-1} \cdot y^{-1}$ with an annual total erosion in the SRYR of 225.18 $\times$ 10^6 $t \cdot y^{-1}$. Spatial analysis revealed that 78.64% of the region suffered low erosion, with erosion intensity declining from northwest to southeast. (3) The annual SEM in the SRYR demonstrated a downward trend from 2001 to 2020, with 83.43% of the study area showing improvement. Based on these findings, measures for soil erosion prevention and control in the SRYR were proposed. Future studies should refine the temporal analysis to better understand the influence of extreme climate events on soil erosion, while leveraging high-resolution data to enhance model accuracy. Insights into the drivers of soil erosion in the SRYR will support more effective policy development.

Keywords: soil erosion; ^{137}Cs tracer; random forest; the source region of the Yellow River

check for updates

Citation: Su, J.; Tang, R.; Lin, H. Simulation and Spatio-Temporal Analysis of Soil Erosion in the Source Region of the Yellow River Using Machine Learning Method. *Land* **2024**, *13*, 1456. https://doi.org/10.3390/land13091456

Academic Editor: Hanoch Lavee

Received: 6 August 2024
Revised: 2 September 2024
Accepted: 5 September 2024
Published: 7 September 2024

Copyright: © 2024 by the authors. Licensee MDPI, Basel, Switzerland. This article is an open access article distributed under the terms and conditions of the Creative Commons Attribution (CC BY) license (https://creativecommons.org/licenses/by/4.0/).

1. Introduction

Soil erosion significantly contributes to global land degradation, leading to the loss of soil nutrients and negatively impacting soil-related ecosystems, ultimately threatening regional ecological security [1]. The source region of the Yellow River (SRYR), located in the northeastern part of the Qinghai-Tibet Plateau [2], is often known as the "Chinese Water Tower". It is a vital water source and an important ecological conservation area within the Yellow River Basin [3], serving as a crucial ecological barrier and grassland ecosystem in China [4]. However, due to the combined impacts of human activities and climate change, the SRYR suffers from widespread soil erosion, particularly erosion caused by water, wind, and freeze–thaw cycles [5], and rainfall erosion in this region has also intensified significantly since 1971 [6]. Additionally, the region experiences average wind speeds ranging from 0.6 to 4.2 m/s, which are significantly higher than in neighboring

areas [7], thereby raising the potential for soil erosion. Studies have demonstrated that between 1950 and 2007, the average annual soil erosion modulus (SEM) in the SRYR stood at 18.68 $t \cdot ha^{-1} \cdot y^{-1}$, which represents a notable increase compared to pre-1950 levels [8]. Soil erosion has also exacerbated ecosystem degradation and led to a decline in water quality in the SRYR. Furthermore, it has adversely affected animal husbandry, which serves as the predominant source of income for the region's residents, thus affecting their livelihoods. Consequently, there is an urgent requirement to accurately monitor intensity of soil erosion in the SRYR and establish a robust theoretical basis for the formulation of effective soil and water conservation strategies aimed at preventing and controlling soil erosion.

Soil erosion is a multifaceted process, driven by an array of interacting factors such as vegetation coverage, rainfall erosivity, soil texture, wind speed, freeze–thaw cycles, and human activities [5]. Current methods used to study soil erosion mainly include the runoff plot method, tracer methods, and modeling approaches [9]. The runoff plot technique, widely employed to ascertain the SEM of specific plots, while effective in yielding credible results on a small regional scale [10], faces challenges when estimating soil erosion over large scales, such as the SRYR, and does not provide long-term erosion data.

The nuclide tracer methods utilize radionuclides as tracers to delineate the research object. Among these, cesium-137 (^{137}Cs) is currently the most widely used and mature tracer technology [11,12]. As an artificial radionuclide, ^{137}Cs is deposited on the surface with water vapor and is immediately and strongly adsorbed by soil colloid particles. Given that Cs is a highly active alkali metal, positively charged cesium ions are easily adsorbed to negatively charged sites in soil organic matter, and essentially no further exchange reactions occur [13,14]. Therefore, the subsequent migration of ^{137}Cs is governed by the spatial flow and vertical movement of the soil, rather than chemical processes [15–18], making it a valuable tool for tracing soil erosion. This tracing technology has been widely employed to estimate soil erosion across various spatial scales, with applications by Cheikha et al. [19] in northeastern Tunisia, Porto et al. [20] in southern Italy's catchment areas, Li et al. [8] in the Sanjiangyuan national park, and Lu et al. [21] in the Yushu Mountain area of China. Furthermore, Meusburger et al. [22] demonstrated that model-based methods often yield coarse-grained estimates of soil erosion, whereas fallout radionuclide (FRN) methods offer more reliable long-term assessments. Shao et al. [23] applied ^{137}Cs to evaluate the SEM of typical alpine meadows on the Qinghai-Tibet Plateau, revealing a negative correlation between the soil and water loss rates with vegetation coverage.

Given the limitations of runoff plot and tracer methods in terms of scalability and resource intensity [24], various soil erosion research models have been formulated. These include empirical models like the universal soil loss equation (USLE), the revised universal soil loss equation (RUSLE), and the revised wind erosion equation (RWEQ), as well as physical process models like the water erosion prediction project (WEPP) and the Limburg soil erosion model (LISEM) [25–27]. Among these, the RUSLE model and the RWEQ model are frequently utilized in large-scale studies because of their simplicity as well as empirical basis. However, as research deepens, several shortcomings have become apparent: (1) the accuracy of these models depends on site-specific parameters, which are typically calibrated to normal or moderate erosion. In reality, extreme erosion events are frequent, reducing the model's accuracy [28]. (2) The linear assumptions inherent in these models fail to adequately capture complex physical processes under extreme climate conditions [28,29]. (3) The models consider only the inherent parameters of water and wind erosion dynamics, neglecting the interactions of multiple external forces, thereby overlooking compound erosion phenomena [30,31]. This is particularly pertinent in regions like the SRYR, where the variability in environmental factors is significant, including topography, climate, and vegetation. The SRYR encompasses nearly all types of soil erosion forces on land [32]. Therefore, verifying the applicability of classic models and identifying a model suitable for the SRYR is an urgent scientific challenge.

To overcome these challenges and enhance the precision of soil erosion assessments, researchers have increasingly turned to advanced machine learning techniques. Machine

learning technology offers a promising approach by estimating SEM and examining intricate relationships between soil erosion and its contributing factors, proving highly effective for such assessments [33]. Among various algorithms, the random forest (RF) is particularly notable for constructing a diverse array of decision trees during the training process, which alternates the mode of classification classes or average prediction for regression tasks. This ensemble learning approach mitigates overfitting and bolsters generalization. By combining the outcomes of multiple decision trees, RF enhances model robustness and accuracy [34]. Given these characteristics, the RF model has demonstrated superior evaluation performance in assessing soil erosion across diverse geographic regions, including Central Asia [34–37], South Asia [38,39], northern Europe [40,41] hilly areas in southwestern and southern China [42,43], and the Tibetan Plateau [44].

In assessing soil erosion in the SRYR, the runoff plot method has proven insufficient for large-scale studies. The region encompasses nearly all forms of land-based soil erosion, and the traditional model's applicability in this area necessitates further verification. Consequently, there is a critical necessity to establish a soil erosion assessment and prediction model tailored to the SRYR. This research compiled an environmental variable dataset comprising soil factors, meteorological factors, topographic factors, and remote sensing indices. The SEM measured by ^{137}Cs served as the verification basis. The aims of this study were to: (1) identify the most suitable soil erosion evaluation and prediction model by comparing the traditional empirical models with those based on the machine learning algorithms; (2) examine the spatial and temporal distribution of soil erosion in the study area from 2001 to 2020 utilizing the best-fit model and provide a solid foundation for developing soil and water conservation policies tailored in the SRYR.

2. Materials and Methods

2.1. Study Area

The SRYR (Figure 1) refers to the region extending from the source of the Yellow River to the Tangnaihai Hydrological Station, located from 32°30′−35°0′ N, 95°50′−103°30′ E, encompassing an area of roughly 12.2 × 10^4 km^2 [45–47]. Positioned in the northeastern Qinghai-Tibet Plateau, it forms the headwaters of the Yellow River, Asia's third-longest river. The SRYR experiences a plateau continental climate, characterized by decreasing temperatures and precipitation from east to west, with minimal annual temperature variations. The average annual temperature ranges from −1.7 °C to 3.4 °C [47], with temperatures typically above 0 °C from May to September. The average annual freezing period exceeds 160 days for many years [48]. The seasonal and interannual variations of precipitation are significant, with summer and autumn precipitation contributing over 75% of the annual total, averaging 491.8 mm [49]. The region's elevation ranges from 2680 m to 6248 m, featuring a topography dominated by mountains, hills, and basins [50]. The land cover data utilized for this research combined global land cover data at a 30 m spatial resolution (accessed on 28 March 2024, https://www.webmap.cn/mapDataAction.do?method=globalLandCover) with a grassland type survey map of China from the 1980s in ArcGIS. The predominant land cover in the study area consists of grasslands, including alpine meadow (61.40%), alpine grassland (12.04%), and mountain meadow (9.29%), collectively covering 82.73% of the total area. Other land cover types include wetlands (6.56%), barren land (5.52%), and cultivated land (2.11%), with the remaining types covering areas less than 1.0% [51]. The primary land cover types in the SRYR are alpine meadow soil and alpine grassland soil, featuring layers and coarse textures. The soil composition is 14.5% clay, 39.90% silt, and 38.17% gravel [51].

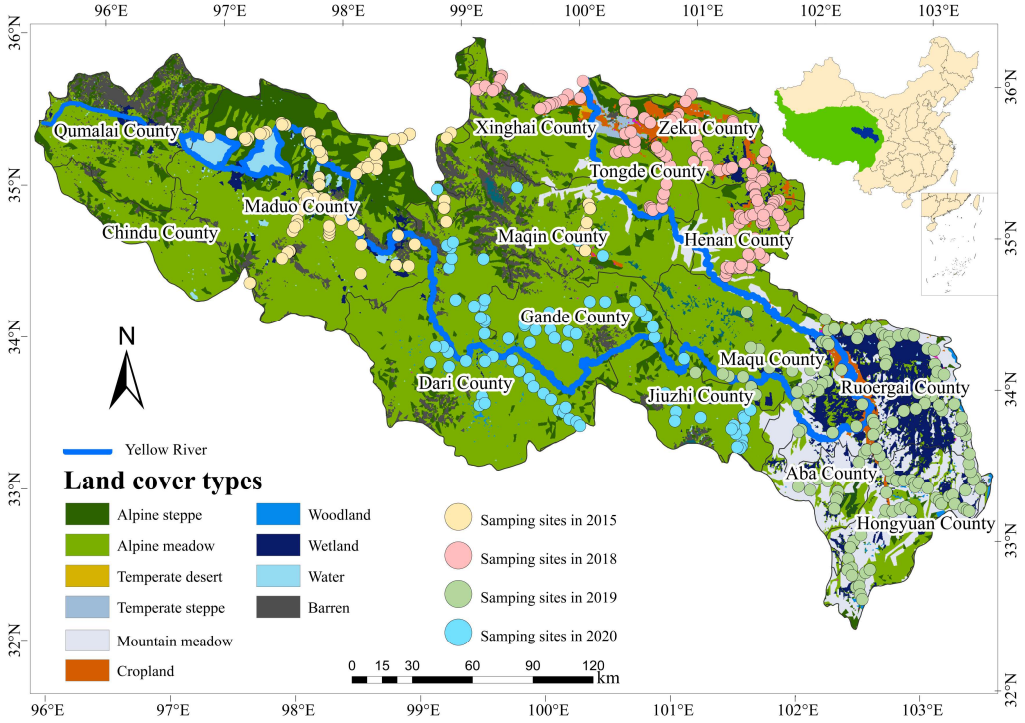


Figure 1. The layout of land cover types and sampling sites from 2015-2020 across the SRYR.

2.2. Data Source and Processing

2.2.1. Measured Data Acquisition and Processing

The soil-measured data play a crucial role in constructing the suitable model in this research. The selection of sampling points for ^{137}Cs needed to represent general characteristics of the SRYR, while also considering practicalities and costs associated with sample collection. To tackle these challenges, the conditional Latin hypercube method (cLHS) [52], constrained by cost layers, was employed to arrange the sample sites. This was implemented by the cLHS tool in RStudio 1.3. A total of 521 soil samples containing ^{137}Cs were gathered across the SRYR between July and August in 2015, 2018, 2019, and 2020. The spatial configuration of these sampling sites is shown in Figure 1. A soil drill with a diameter of 5 cm was employed, targeting the 0–20 cm soil stratum, where over 98% of ^{137}Cs content resides [53]. At each site, 3 replicate samples were taken. The soil samples were then air-dried, ground, and sifted for further analysis. An N-type coaxial high-purity germanium probe, model GMX30P4, was employed for the measurements. Standard source comparison ensured accuracy, with the measurement duration set at 82,800 s. Typically, at a 95% confidence level, the analytical accuracy is approximately ±6%, with spectra interpreted using HPGe Gamma Spectrometer GCW 3523.

The methodology for calculating the SEM for these sampling sites was adapted from Wang et al. [53]. The calculation formula is as follows:

$$\mathrm{SEM} = \frac{\mathrm{CPR} \times \mathrm{BD} \times \mathrm{DI} \times 10^4}{\mathrm{T}} \quad (1)$$

where SEM stands for soil erosion modulus ($t \cdot ha^{-1} \cdot y^{-1}$), CPR indicates change rate of ^{137}Cs during measurement period (%), BD refers to soil bulk density at the sampling sites ($Mg \cdot m^{-3}$), DI represents thickness of the soil layer (m), T denotes the time span from the peak of ^{137}Cs deposition (1963) to the sampling date.

CPR's calculation formula is as follows:

$$\mathrm{CPR} = \frac{(\mathrm{CPI} - \mathrm{CRI}) \times 100}{\mathrm{CRI}} \quad (2)$$

$$CPI = \frac{Ci \times W}{s} \quad (3)$$

where CPI indicates ^{137}Cs concentration in the sample, CRI denotes ^{137}Cs reference inventory (Bq·m^{-2}), Ci represents ^{137}Cs radioactivity (Bq·kg^{-1}), W refers to sample mass (kg), and s is cross-sectional area of the soil drill (m^2).

CRI refers to atmospheric deposition flux of ^{137}Cs per unit area or the undisturbed ^{137}Cs area concentration value [54]. Accurately determining CRI is a prerequisite for using ^{137}Cs tracer technology to measure soil erosion. In this study, CRI was obtained using field exploration sampling and laboratory measurement methods. Typically, there is no erosion and accumulation at the top of the slopes [55]. Thus, the reference inventory site for this study was located at the flat part of the top of the slope, where the vegetation root layer is intact and compact. The sample reference inventory was collected at this location, resulting in 3 reference inventories: 2437.82 Bq·m^{-2}, 2225.42 Bq·m^{-2}, and 2199.61 Bq·m^{-2}. The mean values of these 3 was 2287.44 Bq·m^{-2}, which is consistent with previous studies [56,57].

2.2.2. Environmental Variable Data Acquisition and Processing

Soil erosion is a complex surface phenomenon affected by diverse environmental factors. When selecting variables that impact soil erosion in the SRYR, it is essential to take into account both the existing research basis and the unique characteristics of the SRYR, so as to thoroughly understand influencing mechanisms driving soil erosion in this region. Therefore, this study identified 4 categories of environmental factors, encompassing a total of 34 variables (detailed in Table S1). These factors include:

- Soil factors: 5 variables, including clay, sand, silt, soil organic carbon (SOC), and soil erodibility (K) factor;
- Meteorological factors: 8 variables, including precipitation, temperature, rainfall erosivity (R) factor, wind, illumination, freeze–thaw (FT), nighttime land surface temperature (LsTN), and daytime land surface temperature (LsTD);
- Topographic factors: longitude, latitude, elevation, slope, aspect, and length–slope (LS) factor;
- Remote sensing indices: 15 variables, including enhanced vegetation index (EVI), normalized difference vegetation index (NDVI), coverage, leaf area index (LAI), modified soil adjusted vegetation index (MSAVI), normalized difference vegetation green index (NDVGI), soil adjusted vegetation index (SAVI), difference vegetation index (DVI), normalized difference soil index (NDSI), normalized difference water index (NDWI), optimized soil adjusted vegetation index (OSAVI), ratio vegetation index (RVI), soil adjusted total vegetation index (SATVI), soil color index (SCI), transformed vegetation index (TVI), and coverage.

The data sources for each factor and some data processing methods are presented in Table 1.

Table 1. Data sources and processing.

Variable Types	Data Sources	Data Processing
Soil factors	accessed on 1 April 2024 https://data.isric.org/	-
Meteorological factors	accessed on 1 April 2024 http://data.cma.cn https://data.tpdc.ac.cn/zh-hans/	Meteorological station point data were interpolated into raster data format with a 1 km spatial resolution using ANUSPLIN tool.
Topographic factors	accessed on 15 April 2024 http://srtm.csi.cgiar.org/	Calculated using the DEM and adjusted to a 1 km spatial resolution.
Remote sensing indices	accessed on 28 April 2024 https://code.earthengine.google.com/	-

2.3. Methods and Modeling

2.3.1. RUSLE Model

The revised universal soil loss equation (RUSLE) is a frequently applied method for estimating water erosion [58]. According to Zhao et al. [59], the calculation formula is given as:

$$A = R \times K \times LS \times C \times P \tag{4}$$

where A denotes hydraulic erosion modulus ($t \cdot ha^{-1} \cdot y^{-1}$), R refers to rainfall erosivity factor ($Mj \cdot mm \cdot ha^{-1} \cdot h^{-1} \cdot y^{-1}$), K represents soil erodibility factor ($t \cdot ha \cdot h \cdot Mj^{-1} \cdot mm^{-1}$), LS stands for the length and slope factor, C refers to the vegetation cover management factor, P indicates soil and water conservation practices.

The calculation formulas for the R, K, and C factors are as follows:

$$R = \sum_{j=1}^{12} 1.735 \times 10^{[(1.5 \times \lg \frac{p_j^2}{p}) - 0.8188]} \tag{5}$$

$$K = \left\{0.2 + 0.3\exp\left[-0.0256\mathrm{Sand}\left(1 - \frac{\mathrm{Silt}}{100}\right)\right]\right\} \times \left(\frac{\mathrm{Silt}}{\mathrm{Clay}+\mathrm{Silt}}\right)^{0.3} \times \left[1 - \frac{0.25\mathrm{SOC}}{\mathrm{SOC}+\exp(3.72-2.95\mathrm{SOC})}\right] \times \left[1 - \frac{0.7\mathrm{SN_1}}{\mathrm{SN_1}+\exp(-5.51+22.9\mathrm{SN_1})}\right] \tag{6}$$

$$SN_1 = 1 - \frac{\mathrm{Sand}}{100} \tag{7}$$

$$C = \begin{cases} 1 & VC = 0 \\ 0.6508 - 0.3436\lg(VC) & 0 < VC \leq 78.3\% \\ 0 & VC > 78.3\% \end{cases} \tag{8}$$

$$VC = \frac{NDVI - NDVI_{min}}{NDVI_{max} - NDVI_{min}} \tag{9}$$

where p_j represents monthly rainfall (mm), and p indicates annual rainfall (mm). Sand, Silt, Clay, and SOC represent the respective content percentages in the soil. VC denotes vegetation cover. NDVI was obtained from Google Earth Engine (GEE).

The LS factor was derived from the DEM. The P factor was assigned according to land cover type. Considering that grassland accounts for 82.73% of the study area and human impacts are limited, the P factor was set to 1 [60].

2.3.2. RWEQ Model

The revised wind erosion equation (RWEQ) is a frequently utilized model for estimating wind erosion [61]. According to Teng et al. [62], its calculation formulas are provided as follows:

$$S_L = \frac{2z}{S^2} Q_{max} e^{-(\frac{z}{S})^2} \tag{10}$$

where S_L denotes wind erosion modulus ($t \cdot ha^{-1} \cdot y^{-1}$), z indicates maximum downwind erosion distance (m), S represents potential regional erosion coefficient, Q_{max} signifies maximum potential wind erosion transfer ($kg \cdot m^{-1}$).

S and Q_{max}'s calculation formulas are as follows:

$$S = 150.71(WF \times EF \times SCF \times K' \times C_1)^{-0.3711} \tag{11}$$

$$Q_{max} = 109.8(WF \times EF \times SCF \times K' \times C_1) \tag{12}$$

where WF represents meteorological factor ($kg \cdot m^{-1}$), EF indicates soil erodibility factor ($t \cdot ha \cdot h \cdot Mj^{-1} \cdot mm^{-1}$), SCF denotes soil crust factor, K′ is surface roughness factor, and C_1 is the comprehensive vegetation factor.

WF's calculation formulas are as follows:

$$WF = Wf \times \frac{\rho}{g} \times SW \times SD \quad (13)$$

$$Wf = u_2(u_2 - u_1)^2 \times N_d \quad (14)$$

where Wf denotes wind factor ($m^3 \cdot s^{-3}$), ρ indicates air density ($kg \cdot m^{-3}$), g refers to acceleration due to gravity ($m \cdot s^{-2}$), SW represents soil moisture factor, SD represents snow cover factor, u_2 denotes interpolated wind speed ($m \cdot s^{-1}$), u_1 denotes sand-raising wind speed ($m \cdot s^{-1}$), and Nd represents the number of days with wind speed exceeding 5 $m \cdot s^{-1}$.

EF and SCF's calculation formulas are as follows:

$$EF = \frac{29.09 + 0.31s_a + 0.17s_i + 0.33(\frac{s_i}{c_1}) - 2.59OM - 0.95CACO_3}{100} \quad (15)$$

$$SCF = \frac{1}{1 + 0.0066c_1^2 + 0.021OM^2} \quad (16)$$

where s_a, s_i, c_1, OM, and $CACO_3$ represent the respective contents of sand, silt, clay, organic matter, and calcium carbonate in the soil (%).

K′ and C_1's calculation formulas are as follows:

$$K' = \cos \alpha \quad (17)$$

$$C_1 = e^{-0.0483Coverage} \quad (18)$$

where α denotes the terrain slope, and Coverage indicates the vegetation cover.

2.3.3. Machine Learning Model

There is a high probability of multicollinearity between the environmental variables set previously. Therefore, it is necessary to screen variables before building a model to solve the multicollinearity problem, avoid model complexity caused by information redundancy, and improve model accuracy and computational efficiency [63]. The LASSO algorithm, a linear regression technique used for feature selection, constructs a penalty function to eliminate variables with zero coefficients. This process minimizes the sum of squares of the model residuals, ultimately achieving effective feature selection [64]. The LASSO algorithm demonstrates superior performance when processing high-dimensional remote sensing data [65]. In this study, LASSO was employed to address the issue of multicollinearity among variables.

In recent years, various machine learning algorithms, such as random forest (RF), support vector machine (SVM), K-nearest neighbor (KNN), boosted regression tree (BRT), and extreme gradient boosting (XGBoost), have gained significant traction in research fields like soil erosion and gully erosion [66]. RF, an advanced variant of the decision tree model, leverages advanced non-parametric techniques to surpass the accuracy of other machine learning algorithms [34]. It is recognized as one of the leading machine learning approaches [67,68] and has been extensively utilized for evaluating and predicting soil organic matter, erosion, bedrock depth, as well as soil physical and chemical properties [69]. Two training parameters needed to be set for modeling using the random forest algorithm: the number of regression trees was set to the default value of 500, and the number of randomly selected predictors at each node was set to the square root of the total number of predictors. Then, the relationship between the measured SEM of ^{137}Cs and the erosion influencing factors was modeled to estimate the SEM across the SRYR. The Gini coefficient is used to evaluate the importance of each impacting factor in the RF model. Specifically,

each factor's importance is qualified by calculating impurity reduction when splitting the node [70]. This method aids in identifying the most influential variables affecting soil erosion in the SRYR.

Model performance was assessed through a ten-fold cross-validation approach [70]. Here, 90% of dataset was employed for training and 10% for validation. The R^2 and RMSE were computed for each fold. The RF model's performance was evaluated by averaging the R^2 and RMSE across both training and validation sets over ten iterations.

2.4. Trend Analysis

The Theil–Sen (SEN) median trend analysis and Mann–Kendall test are non-parametric statistical test methods commonly applied in long-term time series data trends [71,72]. Compared with traditional linear trend analysis methods, these approaches offer higher computational efficiency and robustness. Therefore, these methods were employed to determine the soil erosion change trend and significance in the SRYR. When $Sen_{slope} > 0$, it indicates an increasing trend of SEM, reflecting a worsening condition of soil erosion. Conversely, a $Sen_{slope} < 0$ implies an improvement in soil erosion status. The trend's significance was tested at the $\alpha = 0.05$ confidence level. A $z > |1.96|$ signifies a significant change trend ($\alpha < 0.05$), while $z \leq |1.96|$ suggests no significant change ($\alpha < 0.05$). The evaluation standards are shown in Table 2.

Table 2. Standards for assessing change trends in soil erosion in the SRYR.

Sen_{slope}	Z Value	Trends in Soil Erosion
≥0.001	≥1.96	Significantly worsened
≥0.001	−1.96–1.96	Slightly worsened
−0.001–0.001	−1.96–1.96	Stable
≤−0.001	−1.96–1.96	Slightly improved
≤−0.001	≤−1.96	Significantly improved

3. Results

3.1. RUSLE Model Results

The scatter fitting diagram (Figure 2d) reveals that the RUSLE model results did not fit well with the SEM calculated by ^{137}Cs ($R^2 = 0.0082$). The SEM in the SRYR could be classified based on the soil and water loss classification standard (Table S2) issued by the Ministry of Water Resources of the People's Republic of China in 2007 [73]. The annual average SEM in the SRYR calculated by the RUSLE model was 14.81 $t \cdot ha^{-1} \cdot y^{-1}$, contributing to an annual total erosion of 169.04 $\times$ 10^6 $t \cdot y^{-1}$, suggesting that the SRYR experienced low erosion. Specifically, in the northwest and southeast of the SRYR, soil erosion volume was minimal, whereas it was higher in the central areas. The SEM was notably high in Maqin, Dari, Gande, Maqu, Jiuzhi, and Xinghai. The annual average SEM in Jiuzhi, Maqin, and Dari reached 34.51 $t \cdot ha^{-1} \cdot y^{-1}$, 24.14 $t \cdot ha^{-1} \cdot y^{-1}$, and 22.83 $t \cdot ha^{-1} \cdot y^{-1}$, categorizing these areas as moderate-, low-, and low-erosion zones. Overall, the estimation results of the RUSLE model indicated that predominant erosion types in the SRYR were classified as slight and low erosion, constituting 84.35% and 15.57% of the SRYR.

3.2. REWQ Model Results

The scatter fitting diagram (Figure 2e) reveals that the RWEQ model results did not align closely with the SEM calculated by ^{137}Cs well ($R^2 = 0.0301$). The annual average SEM for the SRYR calculated by the RWEQ model was 24.93 $t \cdot ha^{-1} \cdot y^{-1}$, contributing to a total soil loss of 282.83 $\times$ 10^6 $t \cdot y^{-1}$, indicating that the SRYR experienced low erosion. The evaluation results of the RWEQ model were generally higher than those of the RUSLE model and the RF model, with a more dispersed spatial pattern. The RWEQ model identified low and moderate erosion as the predominant types in the SRYR, constituting 44.56% and 51.64% of the SRYR, respectively. Low erosion was mainly concentrated in

Maqin, moderate erosion was spread throughout the SRYR, and high erosion (0.7%) was concentrated at the junction of Xinghai and Tongde.

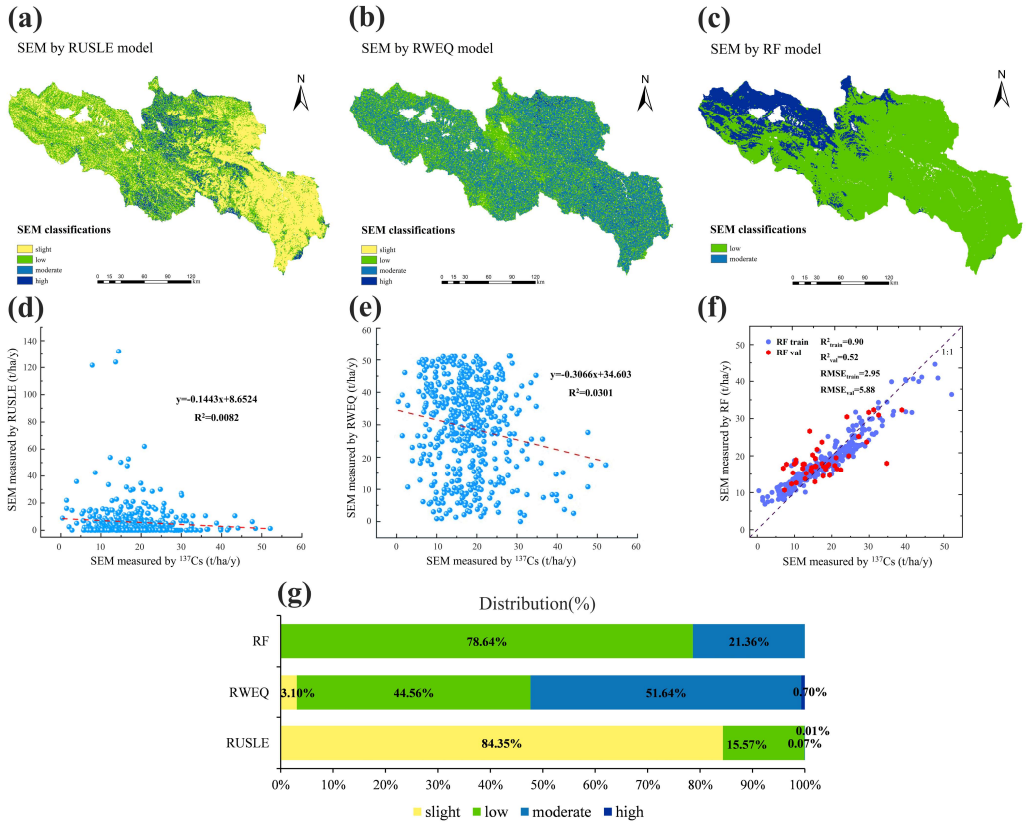


Figure 2. Model results and performance of RUSLE, RWEQ, and RF models: Results of the RUSLE, RWEQ, and RF models (**a**–**c**); Performance of the RUSLE, RWEQ, and RF models (**d**–**f**); Classification of soil erosion for each model (**g**).

3.3. RF Model Results

3.3.1. Variable Selection

The LASSO method was used to select eleven environmental variables, including two soil factors (SOC and clay), three meteorological factors (rainfall, wind, and illumination), two topographic factors (latitude and elevation), and four remote sensing indices (LAI, NDVI, NDSI, and OSAVI). Figure S1 depicts the distribution of the average values of 11 variables over the period from 2001 to 2020. Among these eleven variables, latitude, elevation and clay do not change over time, while the remaining eight variables have values recorded from 2001 to 2020. In total, 163 datasets were applied to the RF algorithm across different years to build a soil erosion evaluation and prediction model.

3.3.2. Model Results and Accuracy Evaluation

As seen from the scatter fitting diagram (Figure 2f), the R^2_{train} value for the training set was 0.9, close to 1, and the RMSE for the training set was 2.95, indicating that the RF model's regression performance was robust and the model was deemed reliable. The annual average SEM in the SRYR calculated by the RF model was 19.32 $t \cdot ha^{-1} \cdot y^{-1}$, contributing to a total erosion volume of 5.18×10^6 $t \cdot y^{-1}$, indicating low erosion in the SRYR. The RF model's classification results for soil erosion in the SRYR were consistent with those from the RUSLE model and the RWEQ model. However, SEM calculated by the RF model fell between those of the RUSLE and the RWEQ model. The SEM in the southeast was low, while it was high in the northwest, indicating a decrease in erosion intensity from northwest to southeast. The SRYR was mainly characterized by low erosion as well as moderate erosion, covering 78.64% and 21.36% of the study area, respectively.

3.4. Spatial Distribution of Soil Erosion in the SRYR

The RF model outperformed the other two models, allowing for a detailed analysis of the spatial and temporal patterns of soil erosion in the SRYR using its estimation results. To effectively utilize the soil erosion simulation outcomes for management purposes, the results were disaggregated by county (Table 3). Among the 15 counties in the SRYR, Qumalai, Maduo, and Chindu reached the highest annual average SEM, at 28.89 $t{\cdot}ha^{-1}{\cdot}y^{-1}$, 25.63 $t{\cdot}ha^{-1}{\cdot}y^{-1}$, and 23.76 $t{\cdot}ha^{-1}{\cdot}y^{-1}$. Both Qumalai and Maduo counties were classified as moderate-erosion areas. Moreover, Maduo, Maqin, and Qumalai counties had the highest total soil erosion, at 52.18 $\times$ 10^6 $t{\cdot}y^{-1}$, 25.36 $\times$ 10^6 $t{\cdot}y^{-1}$, and 22.9 $\times$ 10^6 $t{\cdot}y^{-1}$. Although Chindu had the highest SEM, only part of this county is located in the SRYR, resulting in a relatively low total erosion amount. Conversely, the counties with the lowest mean SEM were Hongyuan, Aba, and Ruoergai, at 13.58 $\times$ 10^6 $t{\cdot}y^{-1}$, 14.04 $\times$ 10^6 $t{\cdot}y^{-1}$, and 14.04 $\times$ 10^6 $t{\cdot}y^{-1}$. The NDVI in these areas was relatively high (Figure S1i), indicating good vegetation coverage. This robust vegetation slowed the scouring effect of water on the soil, while plant roots stabilized the soil, thereby reducing erosion caused by both rain and wind [74].

Table 3. SEM, total erosion volume, and proportion for each county in the SRYR between 2001 and 2020.

County	Max ($t{\cdot}ha^{-1}{\cdot}y^{-1}$)	Min ($t{\cdot}ha^{-1}{\cdot}y^{-1}$)	Mean ($t{\cdot}ha^{-1}{\cdot}y^{-1}$)	Total (10^6 $t{\cdot}y^{-1}$)	Proportion (%)
Maduo	33.52	14.62	25.63	52.18	23.17
Maqin	33.03	14.40	19.06	25.36	11.26
Qumalai	33.60	15.18	28.89	22.90	10.17
Dari	32.30	14.09	17.69	20.46	9.09
Maqu	30.73	13.57	15.53	14.75	6.55
Gande	32.90	14.35	16.45	12.02	5.34
Chindu	33.04	15.06	23.76	10.91	4.84
Xinghai	32.76	14.74	19.97	10.59	4.70
Ruoregai	23.05	12.73	14.96	10.12	4.49
Hongyuan	28.98	12.08	13.58	9.14	4.06
Jiuzhi	32.05	13.44	15.19	9.11	4.05
Tongde	32.56	14.59	17.96	8.13	3.61
Henan	25.04	14.51	15.75	7.75	3.44
Zeku	32.17	14.79	16.23	6.87	3.05
Aba	20.47	12.79	14.04	4.90	2.18

To assess how different cover types resist soil erosion, six main land cover types were selected for analysis (Table 4): alpine grassland, alpine meadow, mountain meadow, cropland, wetland, and barren. Among these, barren land exhibited the highest annual average SEM at 28.15 $t{\cdot}ha^{-1}{\cdot}y^{-1}$, mountain meadow recorded the lowest at 14.31 $t{\cdot}ha^{-1}{\cdot}y^{-1}$. Between 2001 and 2020, the alpine grassland demonstrated both the peak SEM value at 33.52 $t{\cdot}ha^{-1}{\cdot}y^{-1}$ and the lowest value at 12.08 $t{\cdot}ha^{-1}{\cdot}y^{-1}$. Furthermore, the alpine meadow suffered the highest total soil erosion, reaching 135.39 $\times$ 10^6 $t{\cdot}y^{-1}$.

3.5. Temporal Distribution of Soil Erosion in the SRYR

The SEM in the SRYR from 2001 to 2020 ranged between 18.04 $t{\cdot}ha^{-1}{\cdot}y^{-1}$ and 20.12 $t{\cdot}ha^{-1}{\cdot}y^{-1}$, with the highest and lowest values recorded in 2003 and 2018, respectively (Figure 3). During this period, the SEM followed a declining trend. The area of moderate soil erosion decreased by 9833 km^2, while the low-erosion area increased by the same amount. The SEM notably decreased from 2003 to 2005, likely due to the intensive implementation of Chinese government policies, including the "Grain to Green Program", and the soil and water conservation policies initiated in the SRYR since 2003 [75]. From 2006 to 2015, SEM exhibited an up-and-down trend but dropped sharply from 2015 to 2018. This sharp decline may be linked to the second round of grassland ecological compensation pol-

icy implemented by the Chinese government in 2016, which increased subsidies for herders to ban grazing, thus alleviating pressure on grasslands and promoting the restoration of grassland vegetation [76]. The trends and fluctuations of SEM in 15 counties from 2001 to 2020 were consistent with those in the overall SRYR (Figure 4). All counties showed varying degrees of decline around 2016. The downward trend was most pronounced in Hongyuan, Aba, and Chindu. Conversely, the fluctuation trend was smaller in Hongyuan, Ruoergai, and Tongde, while larger fluctuations were observed in Jiuzhi, Qumalai, and Henan. The changing trends and fluctuations of SEM across the six main land cover types from 2001 to 2020 were also consistent with those of the SRYR as a whole (Figure 5). Among these, the downward trend of SEM was most evident in alpine grassland, cropland, and mountain meadow. The fluctuation trend was smallest in cropland and largest in barren land.

Table 4. SEM, total erosion volume and proportion for main land cover types in the SRYR between 2001 and 2020.

Land Cover Type	Max ($t \cdot ha^{-1} \cdot y^{-1}$)	Min ($t \cdot ha^{-1} \cdot y^{-1}$)	Mean ($t \cdot ha^{-1} \cdot y^{-1}$)	Total (10^6 $t \cdot y^{-1}$)	Proportion (%)
Alpine steppe	33.52	12.08	24.74	34.68	15.64
Alpine meadow	33.50	12.23	18.49	135.39	61.08
Mountain meadow	25.95	12.14	14.31	15.60	7.04
Cropland	32.53	13.43	17.10	4.13	1.86
Wetland	33.35	12.34	16.98	12.70	5.73
Barren	33.60	14.25	28.15	17.83	8.04

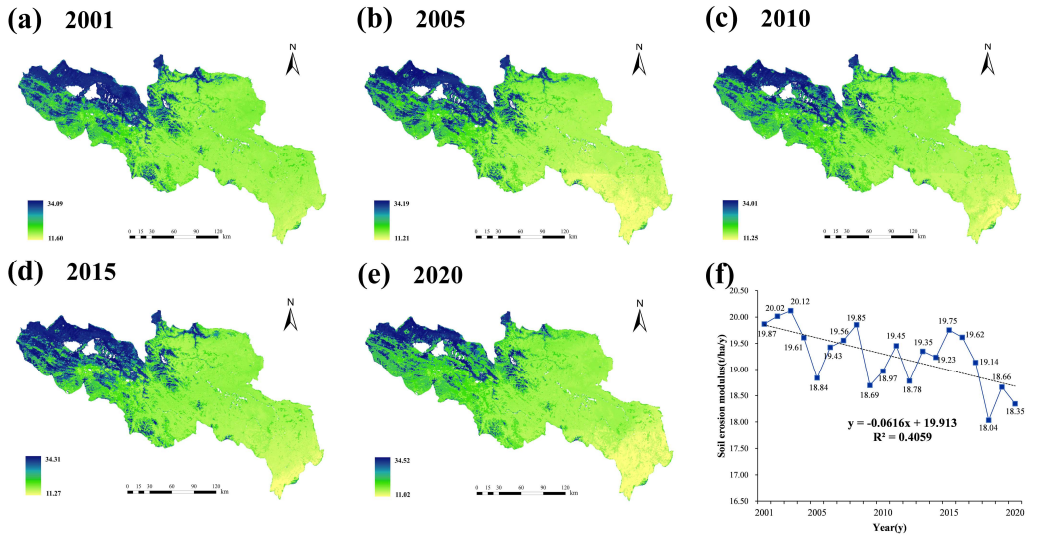


Figure 3. Spatial distribution of SEM in SRYR in 2001 (**a**), 2005 (**b**), 2010 (**c**), 2015 (**d**), 2020 (**e**). Temporal changes of SEM in SRYR between 2001 and 2020 (**f**).

The dynamic trend of soil erosion in the SRYR between 2001 and 2020 (Figure 6) was determined using the Sen trend analysis in conjunction with the Mann–Kendall test. Over the last 20 years, the soil erosion conditions have generally improved in the SRYR. The improved area accounted for 83.43% of the entire study area, with 32.61% of the area showing significant improvement, mainly in the southeast. The slightly improved area accounted for 50.82% and was spread throughout the entire study area. Only 2.07% of the SRYR remained stable, primarily distributed in the northwestern region. Conversely, the area experiencing worsening conditions accounted for 14.5%, with 13.5% undergoing slight worsening, particularly in the northwest of Qumalai, the south of Xinghai, and the east of Maduo and Gande. The significantly worsened areas made up 0.99%, mostly concentrated in the central part of Xinghai.

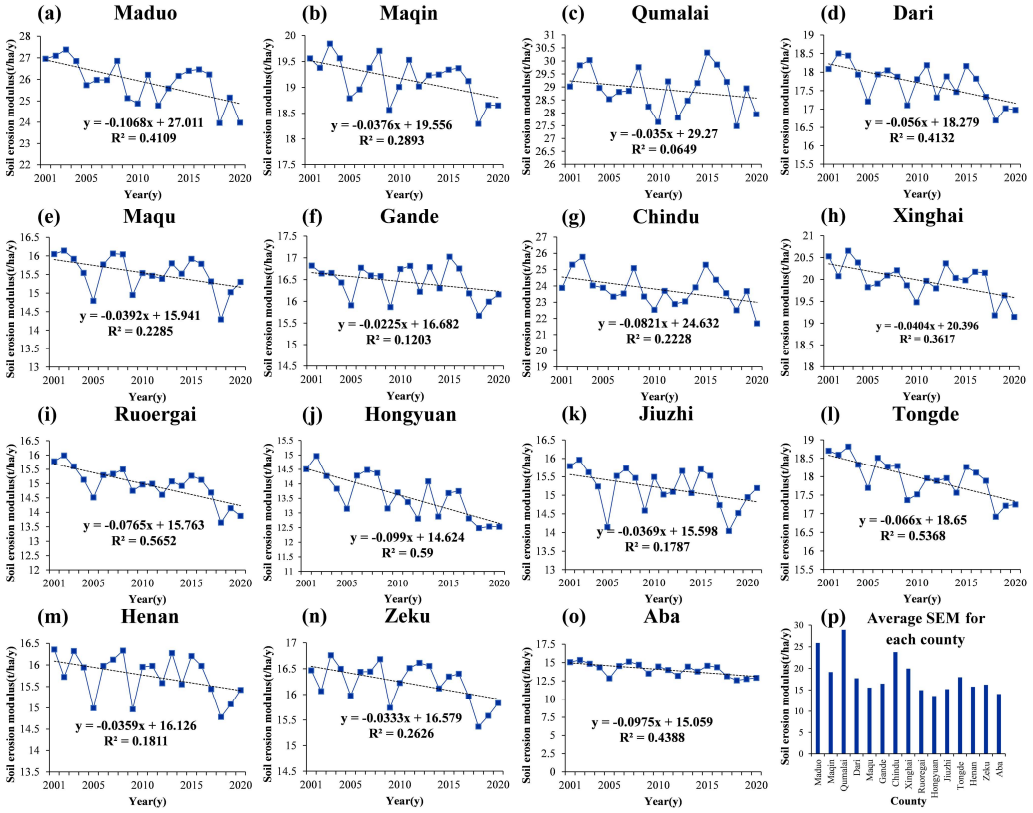


Figure 4. Temporal changes in SEM across each county in the SRYR from 2001 to 2020: Maduo (**a**); Maqin (**b**); Qumalai (**c**); Dari (**d**); Maqu (**e**); Gande (**f**); Chindu (**g**); Xinghai (**h**); Ruoergai (**i**); Hongyuan (**j**); Jiuzhi (**k**); Tongde (**l**); Henan (**m**); Zeku (**n**); Aba (**o**). Average soil erosion modulus for each county from 2001 to 2020 (**p**).

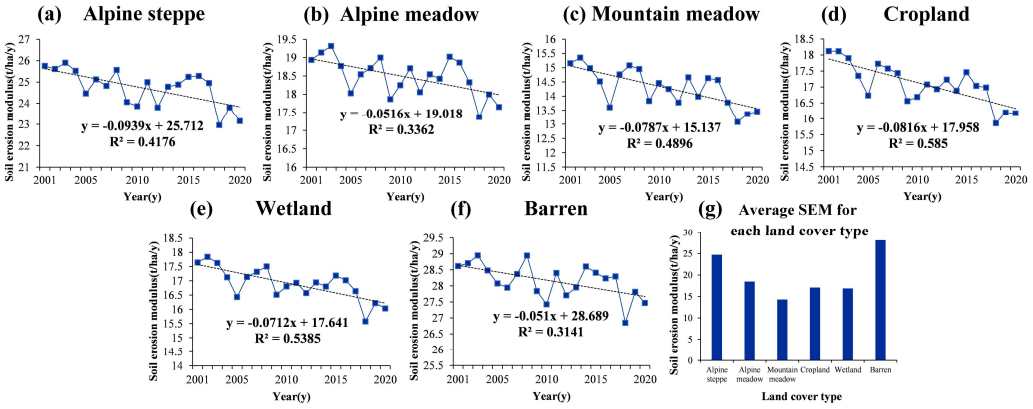


Figure 5. Temporal changes in SEM across main land cover types in the SRYR from 2001 to 2020: Alpine steppe (**a**); Alpine meadow (**b**); Mountain meadow (**c**); Cropland (**d**); Wetland (**e**); Barren (**f**). Average soil erosion modulus for land cover types mentioned above from 2001 to 2020 (**g**).

From the perspective of county administrative divisions (Figure S2a), Hongyuan (93.65%), Aba (86.26%), and Zeku (89.48%) had a significantly higher proportion of improved areas (including both slightly and significantly improved) compared to other counties and the overall average level of the SRYR, which stood at 32.61%. Similarly, counties like Xinghai (8.70%), Qumalai (1.86%), Maqin (1.47%), and Chindu (1.39%) exhibited a higher proportion of worsened areas (including both slightly and significantly worsened) than other counties and the overall SRYR average of 0.99%. Counties where improved soil erosion conditions accounted for over 90% of their total area include Aba (99.69%), Henan (99.59%), Ruoergai (99.49%), Hongyuan (98.9%), Maqu (98.29%), Jiuzhi (98.21%),

and Zeku (94.1%). Meanwhile, counties with improved areas covering 80% to 90% of their land include Dari (85.3%), Maduo (81.44%), and Gande (80.36%). Notably, the proportion of worsened soil erosion exceeded 30% in Xinghai (53.00%) and Qumalai (33.04%), marking these regions as critical zones for erosion control.

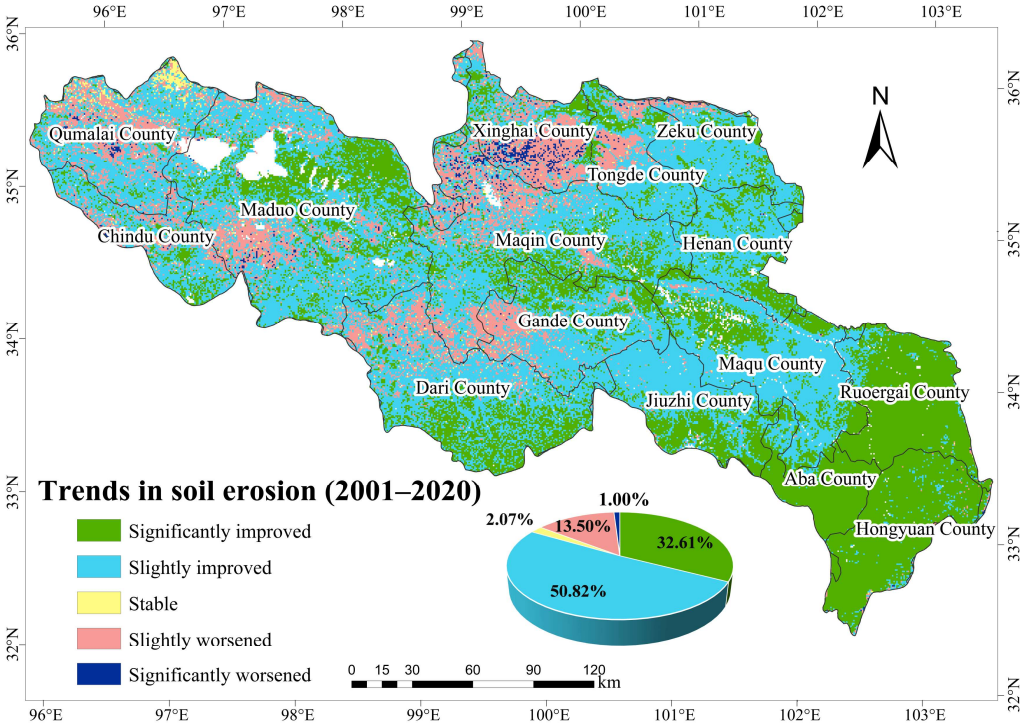


Figure 6. Temporal trends for SEM in the SRYR between 2001 and 2020.

From a land cover perspective (Figure S2b), mountain meadow (71.63%) and wetland (64.92%) had significantly higher proportions of improved areas compared to other land cover types and the SRYR average. In contrast, barren land (1.72%), alpine grassland (1.10%), and alpine meadow (1.04%) showed a higher proportion of significantly worsened areas compared to other land cover types and the SRYR average. The order of soil erosion improvement, from highest to lowest, is as follows: mountain meadow (97.93%), wetland (95.21%), cropland (94.74%), alpine meadow (82.55%), alpine grassland (78.85%), and barren land (63.83%).

4. Discussion

4.1. Model Comparisons and Effectiveness

From the RUSLE model evaluation and the fitting scatter plot of the SEM calculated by ^{137}Cs (Figure 2d), it is evident that the model performed poorly for soil erosion in the SRYR (R^2 = 0.0082). The possible reasons are as follows: firstly, the RUSLE model operates as a linear model. According to the calculation formula of the C factor (Figure S3a), when vegetation coverage (VC) is greater than 78.3%, the C factor result is 0. The VC in the southeastern SRYR (Figure S1i) was relatively high. Therefore, when the RUSLE model was applied to estimate the SEM in the SRYR, the fitting results for Hongyuan, Aba, and Ruoergai in the southeast were close to 0 $t \cdot ha^{-1} \cdot y^{-1}$. Notwithstanding, soil loss still occurs under heavy rainfall or extreme climate conditions, despite high vegetation coverage. Secondly, the LS factor (Figure S3b) was minimal and close to 0 in the northwest, which also made the SEM in Maduo and Qumalai close to 0 $t \cdot ha^{-1} \cdot y^{-1}$. The LS factor calculation assumes uniform slope, neglecting slope shape and terrain complexity, contributing to model error [77]. Additionally, R factor (Figure S3c) in this study was found to be negatively correlated with soil erosion, which contradicts the theoretical basis of the RUSLE model.

The discrepancy might be due to utilizing monthly rainfall data rather than cumulative heavy rainfall data for calculating the R factor.

From the fitting scatter plot of the RWEQ model evaluation results and the SEM estimated by ^{137}Cs (Figure 2e), it is evident that the performance (R^2 = 0.0301) was better than that of the RUSLE model, but still poor. In this study, annual rather than monthly meteorological data were used in the RWEQ model for evaluation, failing to capture the monthly variations in meteorological factors [78], which is the primary reason for the model's deviation. Additionally, a study on wind erosion in the Tarim Basin of China and the Columbia Plateau of the United States indicated that even after calibrating the empirical parameters of the RWEQ model, its performance remained poor. This was likely due to the model underestimating the maximum potential wind erosion [79].

The SEM calculated by ^{137}Cs was used to establish and verify a custom soil erosion evaluation and prediction model, and the findings revealed that, in the SRYR, the soil erosion types primarily consisted of low erosion and moderate erosion. Between 2001 and 2020, the proportion of moderate erosion decreased, while the corresponding share of low erosion increased. These findings align with the conclusions of Li et al. [80], Li et al. [81], and Yin et al. [82]. Soil erosion peaked in the northwest and gradually diminished toward the southeast, consistent with the findings of Xiao et al. [83]. Moreover, sediment serves as a crucial indicator for assessing land degradation and erosion within a watershed. It is driven by factors such as rainfall, runoff, and other processes that erode soil particles from the surface [84]. The findings of this study are validated against monitoring data from the Tangnaihai Hydrological Station, situated downstream of the SRYR. In 2020, the station recorded an annual sediment delivery of 18.8×10^6 t·y^{-1} [85], while total erosion in the SRYR estimated by the RF model is 214.4×10^6 t·y^{-1}, resulting in a sediment delivery ratio (SDR) of 0.088. The SDR aligns closely with values calculated in previous studies for the Tangnaihai Hydrological Station [86]. Thus, the custom soil erosion model established is considered to be more reliable.

4.2. Influence Factors

The RF algorithm's feature importance results highlighted NDVI as the most significant factor influencing soil erosion in the SRYR (Figure S4), aligning with the findings by Wang et al. [87] and Yin et al. [82]. This research reported a negative correlation coefficient of −0.46 between NDVI and the SEM by ^{137}Cs. The higher the NDVI, the lower the SEM. NDVI, OSAVI, and LAI can all reflect the coverage and reproduction of vegetation. The OSAVI and LAI were also negatively correlated with the SEM, both showing a correlation coefficient of −0.42. In general, the surface layer of vegetation can effectively intercept and dissipate raindrops, and the root system can prevent the generation of surface runoff, thereby improving the resistance of soil to water erosion [88]. Meanwhile, vegetation coverage can reduce wind erosion by reducing wind speed and fixing sand and dust [89]. Precipitation ranked second in the importance of features in the RF algorithm (Figure S4). In this study, it was negatively correlated with the SEM calculated by ^{137}Cs (−0.37). This observation aligns with results from Zhang et al. [90] in central Oklahoma and Jobin Thomas et al. [91] in the Pamba River Basin (PRB), India. While many studies have pointed out that precipitation is positively correlated with SEM [92,93], the relationship between rainfall and soil erosion exhibited complexity. Appropriate rainfall helps to form the surface structural sealing effect of the soil and reduces the SEM [94]. However, it is worth noting that the intensity and duration of rainfall influence how precipitation affects soil erosion. The rainfall intensity and duration in the SRYR are smaller than those in southern China, where there are continuous and concentrated rainstorms. Low-intensity precipitation promotes soil moisture infiltration, reduces surface runoff [95], and provides favorable natural conditions for vegetation growth, slowing down soil erosion. Therefore, future research should incorporate analysis on a monthly scale, focusing on extreme climatic events like storms, to further understand rainfall's impact on soil erosion [96], and use the heavy rainfall accumulation to characterize rainfall erosivity. Although altitude was not

identified as the most significant factor for soil erosion in this study (Figure S4), it is crucial to recognize that its importance can vary in other studies. The impact of soil erosion factors often depends on regional characteristics and the scale of research [97]. The 30 m resolution DEM data employed here may have limited the depiction of large-scale terrain changes, affecting altitude's role in explaining erosion. Future research should investigate the influence of terrain factors at varying spatial resolutions for a more comprehensive understanding.

A positive correlation between altitude and SEM was also found, consistent with findings by Nearing et al. [98]. This may be due to vegetation coverage being the most crucial factor affecting soil erosion in the SRYR. High-altitude areas have limited vegetation growth due to climatic conditions, making soil more prone to direct erosion from runoff and raindrops [99]. Li et al. found that altitude was a key factor influencing gully erosion in the Lhasa River Basin, where higher altitude was linked to a lower risk of gully erosion, attributed to larger catchment areas as well as increased kinetic energy of runoff at lower elevations [100]. Finally, soil components like SOC and clay contribute significantly by promoting soil stability and enhancing water retention, thus mitigating the effects of water flow [101]. NDSI, indicative of soil moisture, organic content, and structure, is inversely related to SEM. Further research should delve into how these soil properties influence erosion through empirical fieldwork and lab-based studies.

4.3. Implications for Soil Erosion Prevention and Control in the SRYR

The spatial and temporal patterns of soil erosion in the SRYR provide critical insights for developing soil erosion prevention and control strategies. Firstly, the magnitude of soil erosion and its trends should serve as the basis for classification, enabling prioritized management across counties with zoning and hierarchical strategies. Maduo, Chindu, and Qumalai counties require more intensive soil erosion control, with average SEM values of 28.89 $t \cdot ha^{-1} \cdot y^{-1}$, 25.63 $t \cdot ha^{-1} \cdot y^{-1}$, and 23.76 $t \cdot ha^{-1} \cdot y^{-1}$. Additionally, Qumalai and Chindu counties had significantly worsened soil erosion areas larger than the SRYR average (0.99%), at 1.86% and 1.39, respectively. They showed lower NDVI, OSAVI, and LAI values, higher NDSI, lower vegetation coverage, poorer soil conditions, and less precipitation compared to other counties (Figure S1). Consequently, revegetation measures are essential for erosion mitigation. Specifically, strict adherence to grazing bans during the greening period from early May to late June each year, the most fragile time for the SRYR ecosystem [102], can enhance pasture growth and increase vegetation coverage and biomass. In economically better-off areas, initiatives such as water diversion projects and artificial rainfall can aid in irrigating grasslands and restoring vegetation. Conversely, Hongyuan, Zeku, and Aba counties had lower soil erosion control needs, with the lowest annual average SEM values at 12.08 $t \cdot ha^{-1} \cdot y^{-1}$, 12.73 $t \cdot ha^{-1} \cdot y^{-1}$, and 12.79 $t \cdot ha^{-1} \cdot y^{-1}$ (Table 3). Their proportion of areas with significantly improved soil erosion was much higher than that of other counties in the SRYR, at 93.65%, 89.48%, and 86.26%, respectively (Table S4). For these regions, efforts should focus on enhancing grassland productivity by selecting grass species with strong climate adaptability and high yields, adhering to grass–livestock balance standards, and reducing grazing pressure on natural grasslands. The other nine counties had moderate soil erosion control demands. In these regions, the optimal grazing rate can be determined based on the pasture yields in low-yield years. Additionally, in regions with higher altitudes and severe rain erosion, biological measures and engineering measures can be implemented. Combined with small watershed management projects, these measures can mitigate losses caused by wind and water erosion.

Secondly, counties can implement soil erosion control measures tailored to their predominant land cover types within their regions. The annual average SEM on barren land was the highest, at 28.15 $t \cdot ha^{-1} \cdot y^{-1}$, with significantly worsened soil erosion on barren land accounting for 1.72% of the total study area (Table S4), making it the most impacted land cover type. There is a significant amount of barren land in northern Qumalai and western Maqin (Figure 1). To mitigate soil erosion, these areas should be strategically reclaimed, particularly in the relatively flat river valleys [103]. Finally, this research highlighted the

effectiveness of the Chinese government's soil conservation and ecological restoration initiatives in reducing erosion in the study area. SEM in the 15 counties declined after 2003 but rebounded slightly after 2005 (Figure 4), indicating the successful impact of "Grain to Green Program" since its intensive launch in 2003. Moreover, SEM decreased sharply around 2016 (Figure 4), reaching its lowest value in the entire study period around 2018. This decline may be attributed to the grassland ecological compensation policy implemented by the Chinese government in 2016. Continuing these efforts with consistent policy implementation is vital for sustainable long-term benefits.

5. Conclusions

This research led to the following conclusions:

(1) The RF-based custom soil erosion model outperforms the classical RUSLE model and the RWEQ model in evaluating the soil erosion in the SRYR.

(2) The SRYR experiences distinct spatial and temporal patterns of soil erosion, with erosion intensity diminishing from the northwest to the southwest. Over the period from 2001 to 2020, there has been a general decrease in soil erosion levels.

(3) NDVI emerged as the most critical factor in the RF algorithm, greatly influencing the SEM in the SRYR.

(4) Implementing zoning and hierarchical management strategies for soil erosion prevention and control is essential across the SRYR's counties. Furthermore, barren land can be reclaimed effectively to enhance soil and water conservation.

Although numerical differences exist between the RF soil erosion model's results and classic models, the temporal trends and spatial patterns of soil erosion in the SRYR have been validated in related studies. Moving forward, improving accuracy will require the use of higher-precision environmental data and refined model parameters. Additionally, it will be essential to examine the impact of extreme climate events on soil erosion and to expand the research scale from annual to quarterly and monthly intervals. Investigating the driving factors of soil erosion in the SRYR will provide a more robust theoretical foundation for policy formulation.

Supplementary Materials: The following supporting information can be downloaded at: https://www.mdpi.com/article/10.3390/land13091456/s1, Figure S1: Variables filtered by the LASSO method; Figure S2: Distribution of soil erosion change trends for each county and main land cover types; Figure S3: Spatial distribution of C, LS, and R factor of RUSLE model; Figure S4: Feature importance of influence factors in RF model. Table S1: Variable settings, data sources, and processing; Table S2: Classification standard of soil erosion; Table S3: Distribution of soil erosion change trends for each county in the SRYR; Table S4: Distribution of soil erosion change trends for main land cover types in the SRYR.

Author Contributions: Conceptualization, J.S. and R.T.; methodology, J.S. and H.L.; software, J.S. and R.T.; validation, J.S. and R.T.; formal analysis, J.S. and R.T.; investigation, J.S. and R.T.; resources, H.L.; data curation, J.S. and R.T.; writing—original draft preparation, J.S.; writing—review and editing, J.S.; visualization, J.S. and R.T.; supervision, H.L.; project administration, H.L.; funding acquisition, H.L. All authors have read and agreed to the published version of the manuscript.

Funding: This research was funded by the National Natural Science Foundation of China (32171680 and 31772666), and the Key Consulting Project of the Chinese Academy of Engineering (2020-XZ-29).

Data Availability Statement: All data used in this study are included in the article.

Acknowledgments: The authors express their gratitude to the editor and the anonymous reviewers for their insightful comments and constructive feedback, which significantly enhanced the quality of this paper.

Conflicts of Interest: The authors have no conflicts of interest to declare.

References

1. Zhao, W.W.; Liu, Y.; Daryanto, S.; Fu, B.J.; Wang, S.; Liu, Y.X. Metacoupling supply and demand for soil conservation service. *Curr. Opin. Environ. Sustain.* **2018**, *33*, 136–141. [CrossRef]
2. Dong, S.K.; Wen, L.; Li, Y.Y.; Wang, X.X.; Zhu, L.; Li, X.Y. Soil-Quality Effects of Grassland Degradation and Restoration on the Qinghai-Tibetan Plateau. *Soil Sci. Soc. Am. J.* **2012**, *76*, 2256–2264. [CrossRef]
3. Yi, X.S.; Li, G.S.; Yin, Y.Y. The impacts of grassland vegetation degradation on soil hydrological and ecological effects in the source region of the Yellow River—A case study in Junmuchang region of Maqin country. *Procedia Environ. Sci.* **2012**, *13*, 967–981. [CrossRef]
4. Liu, J.; Sisk, J.M.; Gama, L.; Clements, J.E.; Witwer, K.W. Tristetraprolin expression and micro RNA-mediated regulation during simian immunodeficiency virus infection of the central nervous system. *Mol. Brain* **2013**, *6*, 40. [CrossRef]
5. Jin, F.; Yang, W.; Fu, J.; Li, Z. Effects of vegetation and climate on the changes of soil erosion in the Loess Plateau of China. *Sci. Total Environ.* **2021**, *773*, 145514. [CrossRef] [PubMed]
6. Wang, W.; Yin, S.; Gao, G.; Papalexiou, S.M.; Wang, Z. Increasing trends in rainfall erosivity in the Yellow River basin from 1971 to 2020. *J. Hydrol.* **2022**, *610*, 127851. [CrossRef]
7. Tian, Q.L.; Zhang, X.P.; He, J.; Yi, H.J.; He, L.; Yang, Q.K. Potential risk of soil erosion on the Tibetan Plateau during 1990–2020: Impact of climate change and human activities. *Ecol. Indic.* **2023**, *154*, 110669. [CrossRef]
8. Li, Y.; Li, J.J.; Are, K.S.; Huang, Z.G.; Yu, H.Q.; Zhang, Q.W. Livestock grazing significantly accelerates soil erosion more than climate change in Qinghai-Tibet Plateau: Evidenced from 137Cs and 210Pbex measurements. *Agric. Ecosyst. Environ.* **2019**, *285*, 106643. [CrossRef]
9. Chuenchum, P.; Xu, M.; Tang, W. Predicted trends of soil erosion and sediment yield from future land use and climate change scenarios in the Lancang–Mekong River by using the modified RUSLE model. *Int. Soil Water Conserv. Res.* **2020**, *8*, 213–227. [CrossRef]
10. Cheng, Z.; Yu, B.; Fu, S. An assessment of runoff process-based models for plots in China Loess Plateau. *Sci. Soil Water Conserv.* **2016**, *14*, 10–17. (In Chinese)
11. Navas, A.; Machín, J.; Soto, J. Assessing soil erosion in a Pyrenean mountain catchment using GIS and fallout 137Cs. *Agric. Ecosyst. Environ.* **2005**, *105*, 493–506. [CrossRef]
12. Tuo, D.; Xu, M.; Gao, G. Relative contributions of wind and water erosion to total soil loss and its effect on soil properties in sloping croplands of the Chinese Loess Plateau. *Sci. Total Environ.* **2018**, *633*, 1032–1040. [CrossRef]
13. Ritchie, J.C.; McHenry, J.R. Application of radioactive fallout cesium-137 (Cs-137) for measuring soil erosion and sediment accumulation rates and patterns: A review. *J. Environ. Qual.* **1990**, *19*, 215–233. [CrossRef]
14. Park, S.M.; Alessi, D.S.; Baek, K. Selective adsorption and irreversible fixation behavior of cesium onto 2:1 layered clay mineral: A mini review. *J. Hazard Mater.* **2019**, *369*, 569–576. [CrossRef]
15. International Atomic Energy Agency. *Use of 137Cs in the Study of Soil Erosion and Sedimentation, IAEA-TECDOC-1028*; IAEA: Vienna, Austria, 1998.
16. Van Oost, K.; Quine, T.A.; Govers, G.; De Gryze, S.; Six, J.; Harden, J.W.; Ritchie, J.C.; McCarty, G.W.; Heckrath, G.; Kosmas, C.; et al. The impact of agricultural soil erosion on the global carbon cycle. *Science* **2007**, *80*, 626–629. [CrossRef]
17. Reinhardt, N.; Herrmann, L. Gamma-ray spectrometry as versatile tool in soil science: A critical review. *J. Plant Nutr. Soil Sci.* **2019**, *182*, 9–27. [CrossRef]
18. Hancock, G.R.; Kunkel, V.; Wells, T.; Martinez, C. Soil organic carbon and soil erosion–understanding change at the large catchment scale. *Geoderma* **2019**, *343*, 60–71. [CrossRef]
19. Cheikha, L.B.; El Asmi, A.M.; Gdiri, A.; Oueslati, M.; Attia, R.; Ben Rhouma, A.; Aouadi, T.; Jaoued, M.; Gueddari, M. Soil erosion rates evaluation via 137Cs and RUSLE modeling in the Sigilil watershed (northeastern Tunisia). *Geoderma Reg.* **2023**, *35*, e00714. [CrossRef]
20. Porto, P.; Callegari, G.; Ouadja, A.; Infusino, E. Using Cs-137 measurements and RUSLE model to explore the effect of land use changes on soil erosion and deposition rates in a mid-sized catchment in southern Italy. *Int. J. Sediment Res.* **2024**, *39*, 167–177. [CrossRef]
21. Lu, H.Y.; Li, W.J.; Yu, S.Y. 137Cs-based estimation of soil erosion and organic carbon loss in Alpine Meadow Soil on Tibetan Plateau. *Bull. Soil Water Conserv.* **2023**, *43*, 330–337, 348. (In Chinese)
22. Meusburger, K.; Mabit, L.; Ketterer, M.; Park, J.H.; Sandor, T.; Porto, P.; Alewell, C. A multi-radionuclide approach to evaluate the suitability of (239+240)Pu as soil erosion tracer. *Sci. Total Environ.* **2016**, *566–567*, 1489–1499. [CrossRef] [PubMed]
23. Shao, Q.Q.; Xiao, T.; Liu, J.Y.; Qi, Y.Q. Soil erosion rates and characteristics of typical alpine meadow using 137Cs technique in Qinghai-Tibet Plateau. *Chin. Sci. Bull.* **2011**, *56*, 1708–1713. (In Chinese) [CrossRef]
24. Chappell, A.; Viscarra Rossel, R.A.; Loughran, R. Spatial uncertainty of 137Cs-derived net (1950s–1990) soil redistribution for Australia. *J. Geophys. Res. Earth Surf.* **2011**, *116*, F04015. [CrossRef]
25. Mohammed, S.; Alsafadi, K.; Talukdar, S.; Kiwan, S.; Hennawi, S.; Alshihabi, O.; Sharaf, M.; Harsanyie, E. Estimation of soil erosion risk in southern part of Syria by using RUSLE integrating geo informatics approach. *Remote Sens. Appl. Soc. Environ.* **2020**, *20*, 100375. [CrossRef]
26. Amore, E.; Modica, C.; Nearing, M.A.; Santoro, V.C. Scale effect in USLE and WEPP application for soil erosion computation from three Sicilian basins. *J. Hydrol.* **2004**, *293*, 100–114. [CrossRef]

27. Takken, I.; Beuselinck, L.; Nachtergaele, J.; Govers, G.; Poesen, J.; Degraer, G. Spatial evaluation of a physically-based distributed erosion model (LISEM). *CATENA* **1999**, *37*, 431–447. [CrossRef]
28. Benavidez, R.; Jackson, B.; Maxwell, D.; Norton, K. A review of the (Revised) Universal Soil Loss Equation ((R)USLE): With a view to increasing its global applicability and improving soil loss estimates. *Hydrol. Earth Syst. Sci.* **2018**, *22*, 6059–6086. [CrossRef]
29. Jarrah, M.; Mayel, S.; Tatarko, J.; Funk, R.; Kuka, K. A review of wind erosion models: Data requirements, processes, and validity. *CATENA* **2020**, *187*, 104388. [CrossRef]
30. Zheng, F.L.; Zhang, J.Q.; Liu, G.; Fan, H.; Wang, B.; Shen, H. Characteristics of Soil Erosion on Sloping Farmlands and Key Fields for Studying Compound Soil Erosion Caused by Multi-forces in Mollisol Region of Northeast China. *Bull. Soil Water Conserv.* **2019**, *39*, 314–319. (In Chinese)
31. Zhang, X.M.; Zhang, D.M.; Wang, L.; Zhang, W. Soil Erosion Analysis in the Irtysh River Basin Under the Combined Effects of Rainfall, Snow, Cover and Land Use. *Bull. Soil Water Conserv.* **2022**, *36*, 104–111. (In Chinese)
32. Chen, T.D.; Jiao, J.Y.; Wang, H.L.; Zhao, C.J.; Lin, H. Progress in Research on Soil Erosion in Qinghai-Tibet Plateau. *Acta Pedol. Sin.* **2020**, *57*, 547–564.
33. Zhao, Y.; Meng, X.M.; Qi, T.J.; Qing, F.; Xiong, M.; Li, Y.; Guo, P.; Chen, G. AI-based identification of low-frequency debris flow catchments in the Bailong River basin, China. *Geomorphology* **2020**, *359*, 107125. [CrossRef]
34. Amiri, M.; Pourghasemi, H.R.; Ghanbarian, G.A.; Afzali, S.F. Assessment of the importance of gully erosion effective factors using Boruta algorithm and its spatial modeling and mapping using three machine learning algorithms. *Geoderma* **2019**, *340*, 55–69. [CrossRef]
35. Pourghasemi, H.R.; Sadhasivam, N.; Kariminejad, N.; Collins, A.L. Gully erosion spatial modelling: Role of machine learning algorithms in selection of the best controlling factors and modelling process. *Geosci. Front.* **2020**, *11*, 2207–2219. [CrossRef]
36. Garosi, Y.; Sheklabadi, M.; Conoscenti, C.; Pourghasemi, H.R.; Van Oost, K. Assessing the performance of GIS-based machine learning models with different accuracy measures for determining susceptibility to gully erosion. *Sci. Total Environ.* **2019**, *664*, 1117–1132. [CrossRef]
37. Wang, F.; Sahana, M.; Pahlevanzadeh, B.; Pal, S.C.; Shit, P.K.; Piran, M.J.; Janizadeh, S.; Band, S.S.; Mosavi, A. Applying different resampling strategies in machine learning models to predict head-cut gully erosion susceptibility. *Alex. Eng. J.* **2021**, *60*, 5813–5829. [CrossRef]
38. Bhattacharya, R.K.; Chatterjee, N.D.; Das, K. Linkages between gully erosion susceptibility and hydrological connectivity in Tropical sub-humid river basin: Application of Machine learning algorithms and Connectivity Index. *CATENA* **2024**, *243*, 108186. [CrossRef]
39. Yang, X.; Yang, Q.; Zhu, H.; Wang, L.; Wang, C.; Pang, G.; Du, C.; Mubeen, M.; Waleed, M.; Hussain, S. Quantitative Evaluation of Soil Water and Wind Erosion Rates in Pakistan. *Remote Sens.* **2023**, *15*, 2404. [CrossRef]
40. Lee, S.; Bae, J.H.; Hong, J.; Yang, D.; Panagos, P.; Borrelli, P.; Yang, J.E.; Kim, J.; Lim, K.J. Estimation of rainfall erosivity factor in Italy and Switzerland using Bayesian optimization based machine learning models. *CATENA* **2022**, *211*, 105957. [CrossRef]
41. Fernández, D.; Adermann, E.; Pizzolato, M.; Pechenkin, R.; Rodríguez, C.G.; Taravat, A. Comparative Analysis of Machine Learning Algorithms for Soil Erosion Modelling Based on Remotely Sensed Data. *Remote Sens.* **2023**, *15*, 482. [CrossRef]
42. Ge, Y.; Zhao, L.; Chen, J.; Li, X.; Li, H.; Wang, Z.; Ren, Y. Study on Soil Erosion Driving Forces by Using (R)USLE Framework and Machine Learning: A Case Study in Southwest China. *Land* **2023**, *12*, 639. [CrossRef]
43. Nguyen, K.A.; Chen, W.; Lin, B.-S.; Seeboonruang, U. Using Machine Learning-Based Algorithms to Analyze Erosion Rates of a Watershed in Northern Taiwan. *Sustainability* **2020**, *12*, 2022. [CrossRef]
44. He, W.; Xiao, Z.; Lu, Q.; Wei, L.; Liu, X. Digital Mapping of Soil Particle Size Fractions in the Loess Plateau, China, Using Environmental Variables and Multivariate Random Forest. *Remote Sens.* **2024**, *16*, 785. [CrossRef]
45. Chen, L.; Liu, C.; Hao, F.; Liu, J.Y.; Dai, D. Change of the Baseflow and it's Impacting Factors in the Source Regions of the Yellow River. *J. Glaciol. Geocryol.* **2006**, *02*, 141–148. (In Chinese)
46. Li, L.; Shen, H.; Dai, S. Response of runoff to climate change and its future tendency in the source region of Yellow River. *J. Geogr. Sci.* **2012**, *22*, 431–440. [CrossRef]
47. Yang, Y.H.; Qin, T.L.; Yan, D.H.; Liu, S.; Feng, J.; Wang, Q.; Liu, H.; Gao, H. Analysis of the evolution of ecosystem service value and its driving factors in the Yellow River Source Area, China. *Ecol. Indic.* **2024**, *158*, 111344. [CrossRef]
48. Jia, Y.W.; Gao, H.; Niu, C.W.; Qiu, Y.Q. Impact of climate change on runoff process in headwater area of the Yellow River. *J. Hydraul. Eng.* **2008**, *1*, 52–58. (In Chinese)
49. Wen, L.Y.; Jin, L.J.; Liu, J.; Wang, P. Precipitation Characteristics and Its Meteorological Causes in the Source Region of the Yellow River. *Yellow River.* **2022**, *44*, 21–25, 57. (In Chinese)
50. Zheng, Z.Y.; Lü, M.X.; Ma, Z.G. Climate, Hydrology, and Vegetation Coverage Changes in Source Region of Yellow River and Countermeasures for Challenges. *Bull. Chin. Acad. Sci.* **2020**, *35*, 61–72.
51. Zhao, Y.T. Alpine Grassland Ecological Security Assessment for the Headwaters of the Yellow River, China. Ph.D. Thesis, Lanzhou University, Lanzhou, China, 2021. (In Chinese).
52. Ma, T.; Brus, D.J.; Zhu, A.X.; Zhang, L.; Scholten, T. Comparison of conditioned Latin hypercube and feature space coverage sampling for predicting soil classes using simulation from soil maps. *Geoderma* **2020**, *370*, 114366. [CrossRef]
53. Wang, Y.; Niu, F.; Wu, Q.; Gao, Z.Y. Assessing soil erosion and control factors by radiometric technique in the source region of the Yellow River, Tibetan Plateau. *Quat. Res.* **2014**, *81*, 538–544. [CrossRef]

54. Zhang, W.; Pan, S.; Zhang, K.; Cao, L.; Zhao, J. Study of the Cesium-137 Reference Inventory in the Mainland of China. *Acta Geogr. Sin.* **2015**, *70*, 1477.
55. Funk, R.; Yong, L.; Hoffmann, C.; Reiche, M.; Zhang, Z.D.; Li, J.J.; Sommer, M. Using 137Cs to estimate wind erosion and dust deposition on grassland in Inner Mongolia—Selection of a reference site and description of the temporal variability. *Plant Soil* **2012**, *351*, 293–307. [CrossRef]
56. Zhang, C.; Gong, J.; Zou, X.; Dong, G.; Li, X.; Dong, Z.; Qing, Z. Estimates of soil movement in a study area in Gonghe Basin, north-east of Qinghai-Tibet Plateau. *J. Arid Environ.* **2003**, *53*, 285–295. [CrossRef]
57. Ping, Y.; Zhibao, D.; Guangrong, D.; Xinbao, Z.; Yiyun, Z. Preliminary results of using 137Cs to study wind erosion in the Qinghai-Tibet Plateau. *J. Arid Environ.* **2001**, *47*, 443–452. [CrossRef]
58. Renard, K.G.; Foster, G.R.; Weesies, G.A.; McCool, D.K.; Yoder, D.C. *Predicting Soil Erosion by Water: A Guide to Conservation Planning with the Revised Universal Soil Loss Equation (RUSLE)*; USDA: Washington, DC, USA, 1997.
59. Zhao, Y.T.; Pu, Y.F.; Lin, H.L.; Tang, R. Examining Soil Erosion Responses to Grassland Conservation Policy in Three-River Headwaters, China. *Sustainability* **2021**, *13*, 2702. [CrossRef]
60. Wischmeier, W.H.; Smith, D.D. *Predicting Rainfall Erosion Losses: A Guide to Conservation Planning*; Agriculture Handbook No. 537; U.S. Department of Agriculture: Washington, DC, USA, 1978.
61. Fryrcar, D.W.; Chen, W.N.; Lester, C. Revised Wind Erosion Equation. *Ann. Arid Zone* **2001**, *40*, 265–279.
62. Teng, Y.M.; Zhan, J.Y.; Liu, W.; Sun, Y.; Agyemang, F.B.; Liang, L.; Li, Z. Spatiotemporal dynamics and drivers of wind erosion on the Qinghai-Tibet Plateau, China. *Ecol. Indic.* **2021**, *123*, 107340. [CrossRef]
63. Sahour, H.; Gholami, V.; Vazifedan, M.; Saeedi, S. Machine learning applications for water-induced soil erosion modeling and mapping. *Soil Tillage Res.* **2021**, *211*, 105032. [CrossRef]
64. Ghosh, P.; Azam, S.; Jonkman, M.; Karim, A.; Javed Mehedi Shamrat, F.M.; Ignatious, E.; Shultana, S.; Beeravolu, A.R.; Bosr, A.F. Efficient prediction of cardiovascular disease using machine learning algorithms with relief and LASSO feature selection techniques. *IEEE Access* **2021**, *9*, 19304–19326. [CrossRef]
65. Tesfaye, A.A.; Osgood, D.; Aweke, B.G. Combining machine learning, space-time cloud restoration and phenology for farm-level wheat yield prediction. *Artif. Intell. Agric.* **2021**, *5*, 208–222. [CrossRef]
66. Liu, C.; Fan, H.; Jiang, Y.; Ma, R.; Song, S. Gully erosion susceptibility assessment based on machine learning—A case study of watersheds in Tuquan County in the black soil region of Northeast China. *CATENA* **2023**, *222*, 106798. [CrossRef]
67. Kulimushi, L.C.; Bashagaluke, J.B.; Prasad, P.; Heri-Kazi, A.B.; Kushwaha, N.L.; Masroor, M.; Choudhari, P.; Elbeltagi, A.; Sajjad, H.; Mohammed, S. Soil erosion susceptibility mapping using ensemble machine learning models: A case study of upper Congo river sub-basin. *CATENA* **2023**, *222*, 106858. [CrossRef]
68. Arabameri, A.; Pradhan, B.; Rezaei, K. Gully erosion zonation mapping using integrated geographically weighted regression with certainty factor and random forest models in GIS. *J. Environ. Manag.* **2019**, *232*, 928–942. [CrossRef] [PubMed]
69. Tian, Z.Y.; Liu, F.; Liang, Y.; Zhu, X.C. Mapping soil erodibility in southeast China at 250 m resolution: Using environmental variables and random forest regression with limited samples. *Int. Soil Water Conserv. Res.* **2022**, *10*, 62–74. [CrossRef]
70. Hastie, T.; Tibshirani, R.; Friedman, J. *The Elements of Statistical Learning: Data Mining, Inference, and Prediction*; Springer Series in Statistics; Springer: New York, NY, USA, 2009.
71. Mann, H.B. Nonparametric Tests Against Trend. *Econometrica* **1945**, *13*, 245–259. [CrossRef]
72. Kendall, M.G. *Rank Correlation Methods*, 4th ed.; Charles Griffin: London, UK, 1975; p. 202.
73. Ministry of Water Resources of PR China. *Standards for Classification and Gradation of Soil Erosion (SL 190-2007)*; Ministry of Water Resources of PR China: Beijing, China, 2008.
74. Zhang, X.; Liu, B.; Xie, Y.; Zhang, J. Effects of vegetation coverage on soil erosion control on the Loess Plateau of China: A review. *CATENA* **2021**, *201*, 105301.
75. Wang, S.; Fu, B.; Piao, S.; Lv, Y.H.; Ciais, P.; Feng, X.M.; Wang, Y.F. Reduced sediment transport in the Yellow River due to anthropogenic changes. *Nat. Geosci.* **2016**, *9*, 38–41. [CrossRef]
76. Ma, H.L.; Lin, H.L.; Xiong, X.Y.; Han, X.P. The Impact of the Grassland Ecological Reward Policy on Grassland Vegetation in Qinghai-Tibet Plateau. *Acta Agrestia Sin.* **2021**, *29*, 545–554. (In Chinese)
77. Liu, B.Y.; Nearing, M.A.; Shi, P.J.; Jia, Z.W. Slope length effects on soil loss for steep slopes. *Soil Sci. Soc. Am. J.* **2000**, *64*, 1759–1763. [CrossRef]
78. Youss, E.F.; Visser, S.; Karssenberg, D. Calibration of RWEQ in a patchy landscape; a first step towards a regional scale wind erosion model. *Aeolian Res.* **2012**, *3*, 467–476. [CrossRef]
79. Pi, H.; Sharratt, B.; Feng, G.; Lei, J. Evaluation of two empirical wind erosion models in arid and semi-arid regions of China and the USA. *Environ. Model. Softw.* **2017**, *91*, 28–46. [CrossRef]
80. Li, Y.; Zhang, J.; Zhu, H.; Zhou, Z.; Jiang, S.; He, S.; Zhang, Y.; Huang, Y.; Li, M.; Xing, G.; et al. Soil Erosion Characteristics and Scenario Analysis in the Yellow River Basin Based on PLUS and RUSLE Models. *Int. J. Environ. Res. Public Health* **2023**, *20*, 1222. [CrossRef] [PubMed]
81. Li, H.; Guan, Q.; Sun, Y.; Wang, Q.; Liang, L.; Ma, Y.; Du, Q. Spatiotemporal analysis of the quantitative attribution of soil water erosion in the upper reaches of the Yellow River Basin based on the RUSLE-TLSD model. *CATENA* **2022**, *212*, 106081. [CrossRef]
82. Yin, Z.; Chang, J.; Huang, Y. Multiscale Spatiotemporal Characteristics of Soil Erosion and Its Influencing Factors in the Yellow River Basin. *Water* **2022**, *14*, 2658. [CrossRef]

83. Xiao, Y.; Guo, B.; Lu, Y.; Zhang, R.; Zhang, D.; Wang, Z. Spatial–temporal evolution patterns of soil erosion in the Yellow River Basin from 1990 to 2015: Impacts of natural factors and land use change. *Geomat. Nat. Hazards Risk* **2020**, *12*, 103–122. [CrossRef]
84. Zhang, F.; Zeng, C.; Wang, G.; Wang, L.; Shi, X. Runoff and sediment yield in relation to precipitation, temperature and glaciers on the Tibetan Plateau. *Int. Soil Water Conserv. Res.* **2022**, *10*, 197–207. [CrossRef]
85. Yellow River Conservation Commission of MWR. *Yellow River Sediment Bulletin 2020*; Yellow River Conservation Commission of MWR: Beijing, China, 2021.
86. Wu, A.; Li, T.; Han, P. Relationship between sediment delivery ratio and basin area in Yellow River. *J. Sediment Res.* **2014**, *1*, 61–67.
87. Wang, K.; Zhou, J.; Tan, M.L.; Lu, P.; Xue, Z.; Liu, M.; Wang, X. Impacts of vegetation restoration on soil erosion in the Yellow River Basin, China. *CATENA* **2024**, *234*, 107547. [CrossRef]
88. Gyssels, G.; Poesen, J.; Bochet, E.; Li, Y. Impact of plant roots on the resistance of soils to erosion by water: A review. *Prog. Phys. Geogr.* **2005**, *29*, 189–217. [CrossRef]
89. Munson, S.M.; Belnap, J.; Okin, G.S. Responses of wind erosion to climate-induced vegetation changes on the Colorado Plateau. *Proc. Natl. Acad. Sci. USA* **2011**, *108*, 3854–3859. [CrossRef]
90. Zhang, X.C.; Nearing, M.A. Impact of Climate Change on Soil Erosion, Runoff, and Wheat Productivity in Central Oklahoma. *CATENA* **2005**, *61*, 185–195. [CrossRef]
91. Thomas, J.; Joseph, S.; Thrivikramji, K.P. Estimation of soil erosion in a rain shadow river basin in the southern Western Ghats, India using RUSLE and transport limited sediment delivery function. *Int. Soil Water Conserv. Res.* **2018**, *6*, 111–122. [CrossRef]
92. Huang, C.; Zhou, Z.; Teng, M.; Wu, C.; Wang, P. Effects of climate, land use and land cover changes on soil loss in the Three Gorges Reservoir area, China. *Geogr. Sustain.* **2020**, *1*, 200–208. [CrossRef]
93. Benaud, P.; Anderson, K.; Evans, M.; Farrow, L.; Glendell, M.; James, M.R.; Quine, T.A.; Quinton, J.N.; Rawlins, B.; Rickson, R.J.; et al. National-scale geodata describe widespread accelerated soil erosion. *Geoderma* **2020**, *371*, 114378. [CrossRef]
94. Morgan, R.P.C. (Ed.) Soil Conservation. In *Problems and Prospects*; Wiley: Chichester, UK, 1981; pp. 139–152.
95. Hill, D.E. *Environmental Soil Physics*; Academic Press: San Diego, CA, USA, 1998.
96. Vanmaercke, M.; Chen, Y.; Haregeweyn, N.; De Geeter, S.; Campforts, B.; Heyndrickx, W.; Tsunekawa, A.; Poesen, J. Predicting gully densities at sub-continental scales: A case study for the Horn of Africa. *Earth Surf. Process. Landf.* **2020**, *45*, 3763–3779. [CrossRef]
97. Li, Z.; Liu, W.; Zhang, X.; Zheng, F. Impacts of land use change and climate variability on hydrology in an agricultural catchment on the Loess Plateau of China. *J. Hydrol.* **2009**, *377*, 35–42. [CrossRef]
98. Nearing, M.A.; Unkrich, C.L.; Goodrich, D.C.; Nichols, M.H.; Keefer, T.O. Temporal and elevation trends in rainfall erosivity on a 149 km² watershed in a semi-arid region of the American Southwest. *Int. Soil Water Conserv. Res.* **2015**, *3*, 77–85. [CrossRef]
99. Thapa, P. Spatial estimation of soil erosion using RUSLE modeling: A case study of Dolakha district, Nepal. *Environ. Syst. Res.* **2020**, *9*, 15. [CrossRef]
100. Li, J.; Chen, Y.; Jiao, J.; Chen, Y.; Chen, T.; Zhao, C.; Zhao, W.; Shang, T.; Xu, Q.; Wang, H.; et al. Gully erosion susceptibility maps and influence factor analysis in the Lhasa River Basin on the Tibetan Plateau, based on machine learning algorithms. *CATENA* **2024**, *235*, 107695. [CrossRef]
101. Pan, J.; Liu, C.; Li, H.; Wu, Q.C.; Dong, Z.; Dou, X.H. Soil-resistant organic carbon improves soil erosion resistance under agroforestry in the Yellow River Flood Plain, China. *Agroforest Syst* **2022**, *96*, 997–1008. [CrossRef]
102. Han, B.; Zhou, B.; Zhao, H.; Shi, M.M.; Song, Y.; Niu, D.C.; Fu, H. Relationships between grassland vegetation turngreen and climate factors in the Three-river Resource region. *Acta Ecol. Sin.* **2019**, *39*, 5635–5641. (In Chinese)
103. Xu, E.; Zhang, H. Change pathway and intersection of rainfall, soil, and land use influencing water-related soil erosion. *Ecol. Indic.* **2020**, *113*, 106281. [CrossRef]

Disclaimer/Publisher's Note: The statements, opinions and data contained in all publications are solely those of the individual author(s) and contributor(s) and not of MDPI and/or the editor(s). MDPI and/or the editor(s) disclaim responsibility for any injury to people or property resulting from any ideas, methods, instructions or products referred to in the content.